Small-Scale Forcing of a Turbulent Boundary Layer

by

Thomas Lorkowski

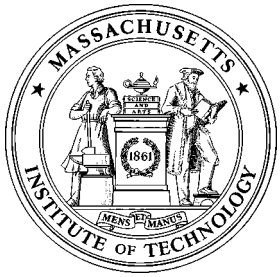

FDRL TR 97-2

Fluid Dynamics Research Laboratory
Department of Aeronautics and Astronautics
Massachusetts Institue of Technology
Cambridge, MA 02139

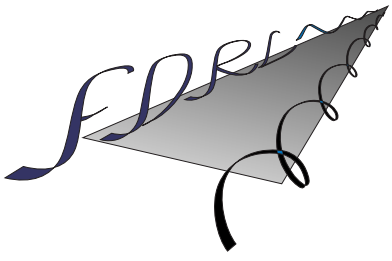

January, 1997

Abstract

In order to understand the effect of small scale forcing on turbulent flows and its implications on control, an experimental investigation is made into the forcing of the inertial scales in the wall region of a turbulent boundary layer. A wall-mounted resonant actuator is used to produce a local vortical structure in the streamwise direction which is convected downstream by the boundary layer flow. The frequency associated with this structure is governed by the resonant frequency of the device and falls in the range of the inertial scales at the Reynolds number of the experiment ($Re_\theta \approx 1200$). Single and multiple point measurements have been made to determine mean and fluctuating statistics as well as dual-point correlations. These data can be used to infer changes in the structure of the near wall region of the boundary layer that are due to the actuator forcing and subsequently, to construct transfer functions between the actuator and the fluid necessary for active control.

This report is the Dipl. Ing. Thesis of Thomas Lorkowski, supervised by Prof. Kenneth Breuer, and submitted to the University of Stuttgart in December, 1996. For more inforation contact: `breuer@mit.edu`

Contents

List of Figures

Chapter 1

Introduction

Coherent structures in turbulent flows are known to be important for turbulent transport. In recent years the active control of such structures has been of considerable research interest for the purpose of drag reduction, noise control, mixing enhancement, and other technologically important applications in aeronautics and turbomachinery. One crucial aspect of the successful implementation of an active control scheme in a turbulent flow is the robust understanding of actuator effects on the structure of the turbulent boundary layer.

Several actuators have been proposed for such turbulent control. One of the most promising is a class of "resonant structural actuators" [1, 2, 3] which introduce disturbances via the resonant vibration of a controlled structure such as a cantileved beam or supported membrane. However, such actuators force the flow at high frequencies (i.e. small scales) which are then "rectified" into larger scale disturbances by viscosity.

In order to understand the effect of such small scale forcing on turbulent flows and its implications for control, an experimental investigation is made on the forcing of the wall region of a turbulent boundary layer using small-scale (high-frequency) resonant actuators. The research program involves the active control of turbulent boundary layers to minimize turbulent pressure fluctuations (responsible for structural vibrations and noise production, and associated with turbulent drag production). This control will be accomplished using wall-mounted sensors and actuators operating in an adaptive feed-forward control loop designed to affect the statistics of the near-wall turbulent boundary layer in a controlled manner. One requirement for the successful design of control algorithms is a clear understanding of the effect that the open-loop operation of the actuator has on the turbulent flow. A series of actuators which are sized to interact with the turbulent flow at a very small scale (1-3 viscous units in width, approximately 100 viscous units in length) have been designed.

A brief review of the theoretical background on turbulent boundary layers and coherent structures is presented in Chapter 2. The experimental setup and the utilized resonant membrane actuator are described in Chapter 3. Implications on the flow statistics as well as the coherent structures when small scale forcing is applied is discussed in Chapter 4 of this paper. The conclusions and an outlook towards the implementation of the results into active feedback control are given in Chapter 5.

Chapter 2

Background

2.1 Incompressible Turbulent Mean Flow

The basic equations of fluid dynamics, namely the continuity equation and the Navier-Stokes equation covering the momentum transport, also characterize turbulent flow. However, the mathematical complexity of turbulence precludes exact analysis. Thus, two approaches are made to describe turbulent flows: statistical theory, which is well developed and will be discussed briefly later in this paper, and on the other hand confining the analysis to mean flow parameters.

2.1.1 The Reynolds Equations

Following the idea of Reynolds (1895), it is assumed that the fluid is in a random unsteady turbulent state. Any variable $Q(t)$ is resolved into a time-averaged mean value $\overline{Q}$ plus a fluctuating value Q', where by definition,

$$\overline{Q} = \lim_{T\to\infty} \frac{1}{T} \int_{t_0}^{t_0+T} Q\,dt, \tag{2.1}$$

and

$$\overline{Q'} = \lim_{T\to\infty} \frac{1}{T} \int_{t_0}^{t_0+T} Q'\,dt = 0. \tag{2.2}$$

Only incompressible turbulent flow with constant transport properties but with possible significant fluctuations in velocity, pressure, and temperature is considered. Introducing a three-dimensional cartesian coordinate system with x in the downstream direction, y normal to the wall, z in spanwise direction, and the velocity components are u,v, and w respectively, this leads to:

$$\begin{aligned} u &= \overline{u} + u' \quad , \quad p = \overline{p} + p' \quad , \\ v &= \overline{v} + v' \quad , \quad T = \overline{T} + T' \quad , \\ w &= \overline{w} + w'. \end{aligned} \tag{2.3}$$

Substituting u, v, and w from Equations (2.3) into the incompressible continuity equation and taking the time average, the result is

$$\frac{\partial \overline{u}}{\partial x} + \frac{\partial \overline{v}}{\partial y} + \frac{\partial \overline{w}}{\partial z} = 0, \tag{2.4}$$

and

$$\frac{\partial u'}{\partial x} + \frac{\partial v'}{\partial y} + \frac{\partial w'}{\partial z} = 0. \tag{2.5}$$

The mean and fluctuating velocity components each separately satisfy an equation of continuity.

The same procedure of substitution is attempted with the nonlinear Navier-Stokes equations. The mean momentum equation is then complicated by a new term involving the turbulent inertia tensor $\overline{u_i' u_j'}$. This new term is never negligible in any turbulent shear flow and introduces nine new variables (the tensor

components). Viewing the turbulent inertia as if they were additional stresses, the mean Navier-Stokes equation is given by

$$\rho \frac{D\overline{\vec{v}}}{Dt} = \rho \vec{g} - \nabla \overline{p} + \nabla \cdot \tau_{ij} \tag{2.6}$$

where

$$\tau_{ij} = \underbrace{\mu \left(\frac{\partial u_i}{\partial x_j} + \frac{\partial u_j}{\partial x_i} \right)}_{laminar} - \underbrace{\rho \overline{u_i' u_j'}}_{turbulent} \quad . \tag{2.7}$$

In a two-dimensional turbulent boundary layer ($\overline{w} = 0$, $\partial/\partial z = 0$), the only significant term reduces to $-\rho \overline{u'v'}$ which is called turbulent shear stress, or Reynolds stress.

2.1.2 Two-Dimensional Boundary Layer Equations

As in laminar boundary layer analysis it is assumed that the boundary layer thickness $\delta(x) \ll x$, which leads to the approximations:

$$\overline{v} \ll \overline{u} \quad , \quad \frac{\partial}{\partial x} \ll \frac{\partial}{\partial y} \tag{2.8}$$

Adopting the two following relations, the mean pressure distribution obtained by the integrated y-momentum equation with Bernoulli's relation at the edge of the layer, and the notation for total shear,

$$\overline{p} = p_\infty(x) - \rho \overline{v'^2} \tag{2.9}$$

and

$$\tau = \mu \frac{\partial \overline{u}}{\partial y} - \rho \overline{u'v'}, \tag{2.10}$$

Equations (2.4) and (2.6) reduce to the following two-dimensional turbulent boundary layer equations:

$$\frac{\partial \overline{u}}{\partial x} + \frac{\partial \overline{v}}{\partial y} = 0, \tag{2.11}$$

and

$$\overline{u} \frac{\partial \overline{u}}{\partial x} + \overline{v} \frac{\partial \overline{u}}{\partial y} = U_\infty \frac{dU_\infty}{dx} + \frac{1}{\rho} \frac{\partial \tau}{\partial y} \tag{2.12}$$

It is assumed that the freestream conditions $U_\infty(x)$ are known and the boundary conditions are met, i.e. no slip, at the wall: $\overline{u}(x,0) = \overline{v}(x,0) = 0$, and free-stream matching: $\overline{u}(x,\delta) = U_\infty(x)$.

2.1.3 Integral Relations for the Turbulent Boundary Layer

The integral relations are formed by using continuity to eliminate $\overline{v}(x,y)$ in favor of $\overline{u}(x,y)$ and then integrating the resulting equations with respect to y across the entire boundary layer. Foremost is the integral momentum relation of von Kármán (1921) which gives the differential equation

$$\frac{d\theta}{dx} + (2+H) \frac{\theta}{U_\infty} \frac{dU_\infty}{dx} = \frac{\tau_w}{\rho U_\infty^2} = \frac{C_f}{2} \tag{2.13}$$

where

$$\text{momentum thickness} \qquad \theta = \int_0^\infty \frac{\overline{u}}{U_\infty} \left(1 - \frac{\overline{u}}{U_\infty} \right) dy,$$

$$\text{shape factor} \qquad H = \frac{\delta^*}{\theta},$$

$$\text{displacement thickness} \qquad \delta^* = \int_0^\infty \left(1 - \frac{\overline{u}}{U_\infty} \right) dy.$$

For a flat plate, where a zero pressure gradient is usually assumed at zero angle of attack, Equation (2.13) reduces to

$$C_f = 2\frac{d\theta}{dx}. \tag{2.14}$$

Prandtl (1927) found a relation between the friction coefficient C_f and θ by assuming that the relations found in pipe-flow experiments, where the skin friction τ_w can easily be determined by the pressure drop, are approximately applicable to plates. This leads to a series of power-law expressions:

$$\begin{aligned} C_f &\approx 0.0592 Re_x^{-\frac{1}{5}}, \\ \frac{\delta}{x} &\approx 0.37 Re_x^{-\frac{1}{5}}, \\ \frac{\theta}{x} &\approx 0.036 Re_x^{-\frac{1}{5}}. \end{aligned} \tag{2.15}$$

Re_x, together with another important Reynolds number based on the momentum thickness θ, are defined by:

$$Re_x = \frac{U_\infty x}{\nu} \quad , \quad Re_\theta = \frac{U_\infty \theta}{\nu}. \tag{2.16}$$

2.1.4 Semitheoretical Considerations

Experimentally-found velocity profiles of turbulent boundary layers are divided into a three-layer concept. The inner layer, closest to the wall, is dominated by viscous shear, whereas the outer layer is dominated by turbulent shear. Between these two layers, in a third layer (the so called overlap layer) both types of shear are important.

For the inner layer, Prandtl proposed that the mean velocity depends only on local properties, that is the wall shear stress τ_w, the fluid physical properties, and the distance y from the wall:

$$\overline{u} = f(\tau_w, \rho, \mu, y). \tag{2.17}$$

Von Kármán suggested for the outer layer, that the wall tends to act as a source of retardation, reducing the local velocity $\overline{u}$ below the freestream value in a manner which is independent of viscosity , μ, but dependent upon the wall shear stress and the distance y:

$$u_\infty - \overline{u} = f(\tau_w, \rho, y, \delta). \tag{2.18}$$

The overlap layer is characterized by fulfilling both the inner and outer law, and the exact form can be determined by dimensional analysis. The proper nondimensionalization of the inner law is

$$\frac{\overline{u}}{u_\tau} = f\left(\frac{y u_\tau}{\nu}\right), \tag{2.19}$$

where

$$u_\tau = \sqrt{\frac{\tau_w}{\rho}}, \tag{2.20}$$

and for the outer law

$$\frac{u_\infty - \overline{u}}{u_\tau} = g\left(\frac{y}{\delta}\right). \tag{2.21}$$

The variable u_τ has units of velocity and is called the skin-friction velocity. The exact forms of the functions f and g are not specified yet. However, it is assumed that in the overlap layer both laws are valid, hence

$$\frac{\overline{u}}{u_\tau} = f\left(\frac{\delta u_\tau}{\nu}\frac{y}{\delta}\right) = \frac{u_\infty}{u_\tau} - g\left(\frac{y}{\delta}\right). \tag{2.22}$$

Mathematically it can be shown that this can be true only if both f and g are logarithmic functions. In the overlap layer, using inner variables, the relation is

$$\frac{\overline{u}}{u_\tau} = \frac{1}{\kappa} \ln \frac{y u_\tau}{\nu} + C. \tag{2.23}$$

Experimental data shows that $(\kappa, C) \approx (0.4, 5.0)$. It is convenient to introduce dimensionless inner variables, denoted by a superscript $+$:

$$\begin{aligned} x^+ &= \frac{x}{l^*} \quad , \quad y^+ = \frac{y}{l^*} \quad , \quad z^+ = \frac{z}{l^*} \\ u^+ &= \frac{u}{u_\tau} \quad , \quad t^+ = \frac{t}{t^*} \end{aligned} \tag{2.24}$$

with

$$l^* = \frac{\nu}{u_\tau} \quad , \quad t^* = \frac{\nu}{{u_\tau}^2} \tag{2.25}$$

where l^* is called the viscous length scale and t^* is the inner time scale. The extent of this logarithmic layer is approximately $30 \leq y^+ \leq 500$. Above that region the outer layer with its turbulent shear becomes dominant and its form is highly dependent on the pressure gradient dp/dx.

Below $y^+ = 30$, the viscous shear becomes dominant and the logarithmic law is not an appropriate way to describe the profile. Very close to the wall, where $\overline{u}, \overline{v}, u', v' \to 0$, the shear stress τ given in Equation (2.10) is reduced to

$$\tau = \mu \frac{\partial \overline{u}}{\partial y} - \underbrace{\rho \overline{u'v'}}_{=0} \approx \tau_w = const. \tag{2.26}$$

Integrating Equation (2.26) leads to the streamwise velocity component $\overline{u}$ as a linear function of the distance to the wall y given by

$$\overline{u} = \frac{\tau_w}{\mu} y = \frac{u_\tau^2 y}{\nu} \tag{2.27}$$

or

$$u^+ = y^+. \tag{2.28}$$

The linear sublayer extents approximately up to $y^+ = 10$. As a summary Figure 2.1 shows the semitheoretical velocity profile of a turbulent boundary layer with the linear sublayer and the adjactent overlap layer following a logarithmic law.

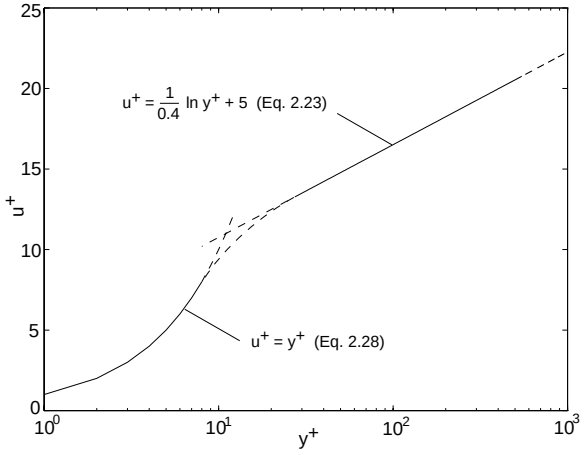

Figure 2.1: Semitheoretical mean velocity profile of a turbulent boundary layer

A much more detailed discussion on turbulent boundary layers, including the energy equations and the resulting thermal boundary layer theory, can be found for example in [4, 5].

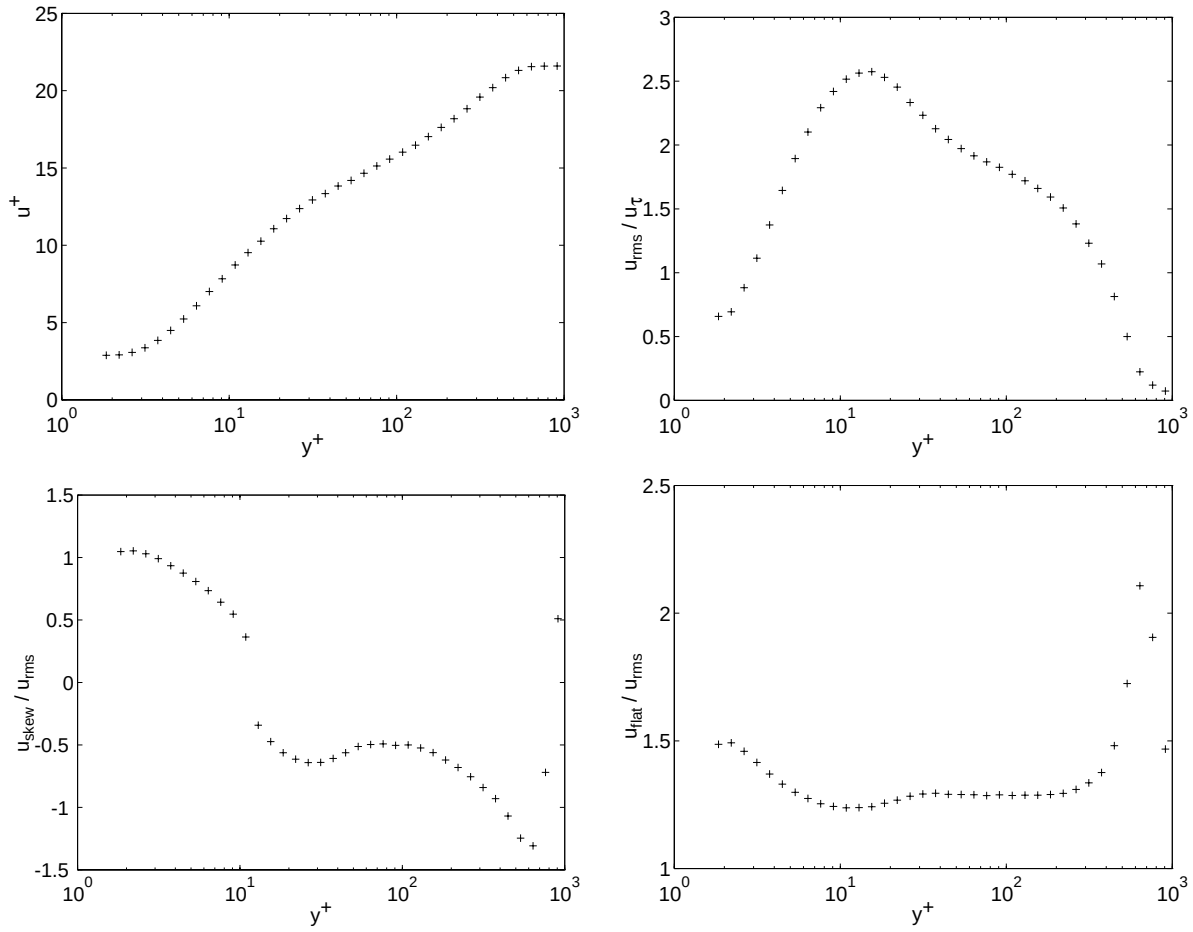

Figure 2.2: Profiles of the first four statistical moments of the streamwise velocity in a turbulent boundary layer ($x^+ = 60$, $z^+ = 0$, unforced)

2.2 Statistical Theory of Turbulence

2.2.1 Fluctuation Analysis

Besides the knowledge of the mean velocity profile discussed in the previous section, it is also import to know the distribution of the fluctuating components across a turbulent boundary layer. Confining the discussion to the streamwise velocity fluctuation u', Equation (2.2) already showed that $\overline{u'} = 0$. The following equation defines the moments up to order $n = 4$:

$$\left(\lim_{T\to\infty} \frac{1}{T} \int_{t_0}^{t_0+T} u'^n dt \right)^{\frac{1}{n}} = \left(\overline{u'^n} \right)^{\frac{1}{n}} = \begin{cases} 0 & n = 1 \\ u_{rms} & n = 2 \\ u_{skew} & n = 3 \\ u_{flat} & n = 4 \end{cases} \tag{2.29}$$

The second order moment, better known as the root-mean-square $\sqrt{\overline{u'^2}}$ (rms) is convenient to measure in experimental investigations and is directly related to such important statistical properties as the standard deviation and probability density distribution of u'.

The higher order moments are utilized for the definition of skewness u_{skew}/u_{rms} and flatness u_{flat}/u_{rms}. Figure 2.2 shows the measured distribution of these four moments across the boundary layer.

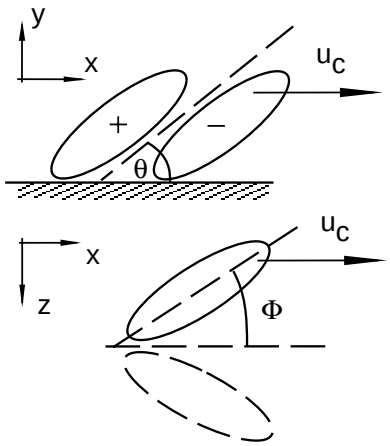

Figure 2.3: Sketch of the attributes of coherent structures in turbulent flow

2.2.2 Coherent Structures in Near-Wall Turbulence

Turbulence appears to be entirely random motion without any possibility to predict the development of flow properties. However, flow visualizations performed by Kline *et.al.* [6] revealed the existence of coherent structures in wall bounded turbulent flow. In the viscous sublayer the near wall flow appears to be made of neighboring regions of high and low velocity (in respect to the mean velocity). These streaks were presumed to be the result of elongated streamwise vortices very near the wall.

If low-speed fluid is lifted up by statistical means into the buffer region, subsequent oscillation and violent breakup into smaller scales (bursting) is coupled to a large part of turbulent production. The variable integral time averaging (VITA) technique developed by Blackwelder and Kaplan [7] is useful to detect these coherent structures in the shear-layer. A bursting event is considered to occur when the short-time variance of the velocity signal exceeds a preset threshold level of the long-term variance. The large-scale organized shear layer structures that evolve out of the lift-up are inclined towards the wall and relatively stable over time and space. Figure 2.3 shows a sketch of the the attributes such as inclination angle and convecting speed of coherent structures in turbulent boundary layer flow. The low-speed fluid lifted up into outer regions is denoted by a minus sign.

Experimental investigations by Johansson, Alfredsson and Eckelmann [8], utilizing two hot-wire probes and the VITA conditional sampling technique for mapping the flow field, resulted in a detailed description of these coherent structures. The maximum inclination angle θ was found to be 20° in the buffer region. The streamwise extent of the coherent structures is about $100\,l^*$, and they retain their nature over a traveling distance of at least $500\,l^*$ with an almost constant propagation speed $u_c = 13\,u_\tau$ up to $y^+ = 30$. The coherent structures were found to be essentially confined within the near-wall region (up to $y^+ \approx 100$). Johansson, Alfredsson and Kim [9] found in numerical simulation a slightly lower propagation speed of $10.6\,u_\tau$ but confirmed the experimental results. The spanwise spacing of these structures is widely agreed to be about $100\,l^*$ [10].

Since these coherent structures play a major role in turbulence production and transport, the sound understanding of the evolution of these structures, especially when being actively manipulated, could lead to active control schemes for turbulence reduction.

Chapter 3

Experimental Setup

All experiments supporting this research were performed in the Low Turbulence Wind Tunnel Laboratory in the Department of Aeronautics and Astronautics at the Massachusetts Institute of Technology.

3.1 Wind Tunnel and Flat Plate

The primary apparatus used to support this research was an open circuit wind tunnel shown in Figure 3.1 [11]. The tunnel is comprised of a 16:1 contraction, followed by an interchangeable test section, diffuser, and fan. Several flow straightening devices have been installed to improve the quality of the flow entering the test section. Bell shaped surfaces were included on three sides of the inlet to reduce inlet separation. A honeycomb structure followed by seamless screens inside the contraction reduced longitudinal and lateral velocity fluctuations.

A precision aluminum flat plate was positioned vertically in the test section and fastened to the floor and ceiling using support brackets (Figure 3.2). The x-direction is defined positive downstream, the y-direction normal to the plate, and the z-direction is in spanwise direction, defined positive towards the floor. A sharp leading edge extension was attached to the front end of the plate and a trailing edge flap was attached to the downstream end to adjust the pressure gradient along the plate. At five locations along the center line, Plexiglas plugs could be removed to hold the actuator equipment. The flow was tripped utilizing a Velcro tape stretched spanwise across the plate 10 cm from the leading edge.

A stepper-motor driven, programmable, three-axis traversing mechanism was installed in the test section for precise and automatic placement of flow measuring instrumentation. The x-traverse provides travel up to 0.70 m, the z-traverse could be positioned within ± 0.35 m from the centerline of the flat plate. Both the x- and z-traverse provided a 0.007 mm resolution. The y-traverse provides positioning up to 0.10 m normal to the flat plate and was geared to give a 0.004 mm resolution [11].

3.2 Membrane Actuator

The actuator device utilized in this study follows the original design of Glezer [2] and incorporates ideas from Jacobson and Reynold [1]. A schematic of the actuator is shown in Figure 3.3. A thin membrane 25.4 mm in diameter was made using a 80 μm thick brass shim bonded at its edges to steel washers. A small rectangular Nickel plated piezo-ceramic was bonded (using epoxy and silver paint) with one short edge rigidly fixed to the edge support. The membrane makes up an end wall of a closed sub-surface cavity. The opposite wall, flush mounted to the plate, is rigid with an exit slit 80 μm wide and 8 mm long ($1.5 \times 150\, l^*$). The slit orientation was with its longer side parallel to the main flow. Working at its resonant frequency (500 Hz, 0.10 f^*), the oscillating pressure in the cavity results in the generation of a pair of counter-rotating vortices introduced by the jet emerging into the flow above the exit slit. Due to the closed cavity, the actuator has an overall zero mass flux.

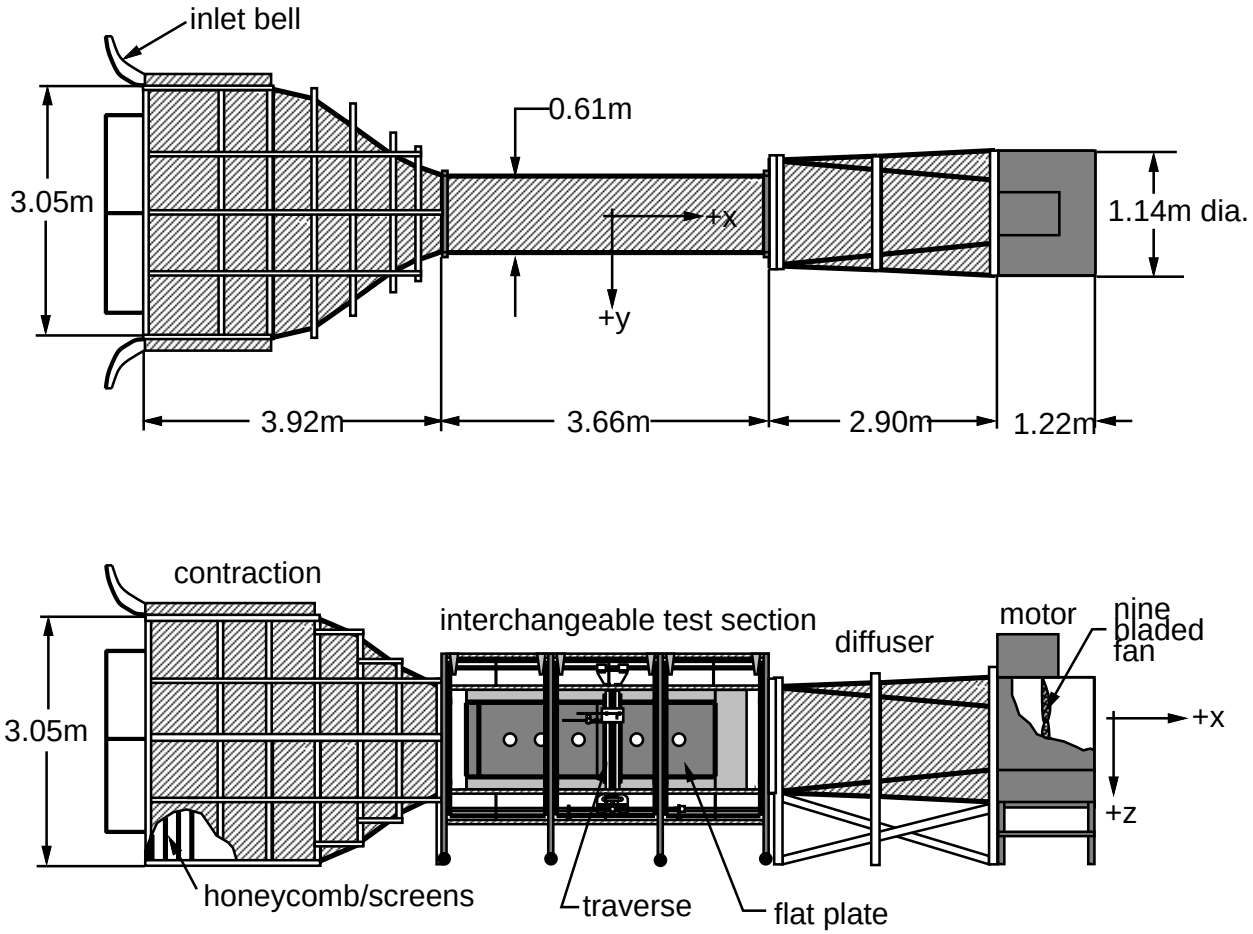

Figure 3.1: Low Turbulence Wind Tunnel, Fluid Dynamics Research Lab, M.I.T.

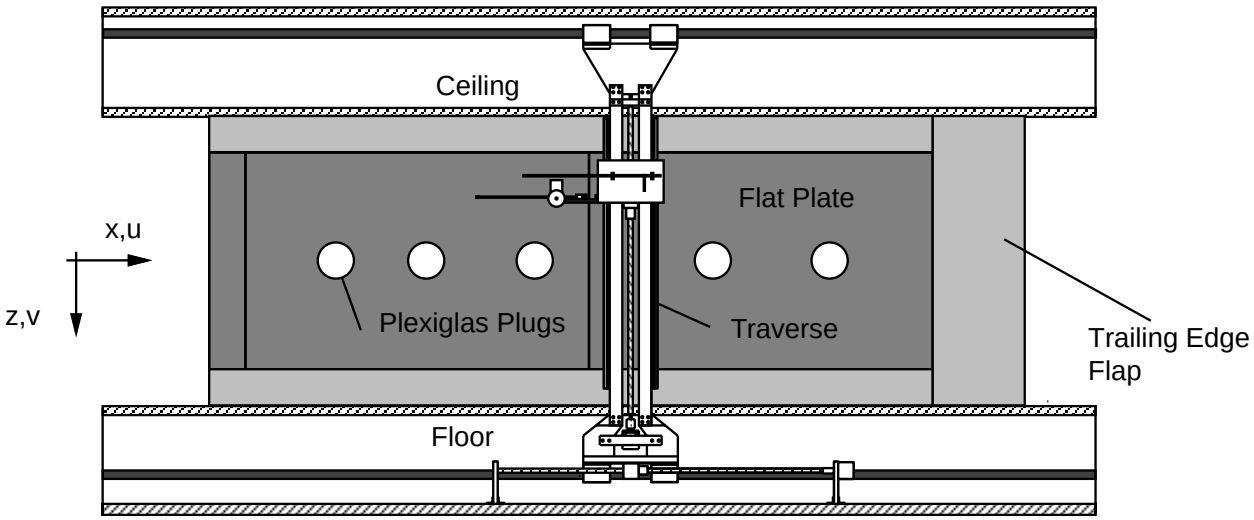

Figure 3.2: Interchangeable test section

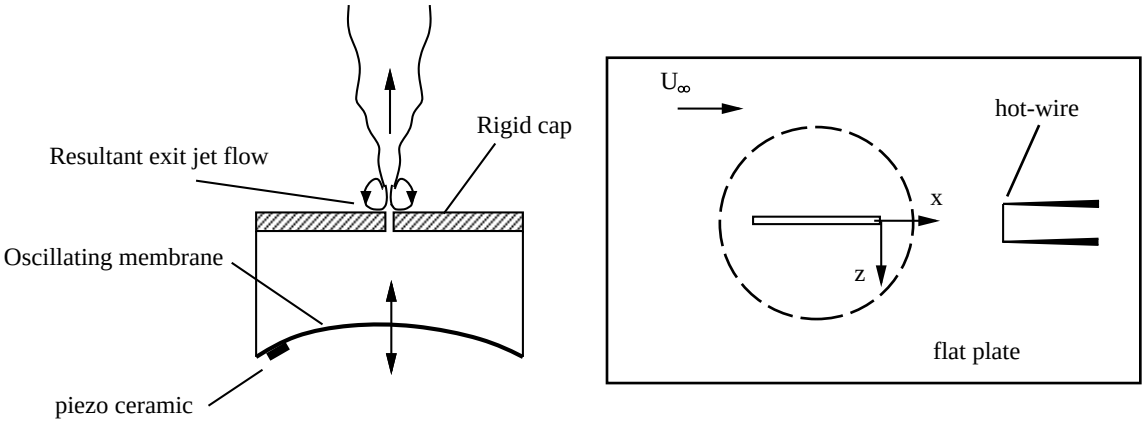

Figure 3.3: Schematic of resonant membrane actuator

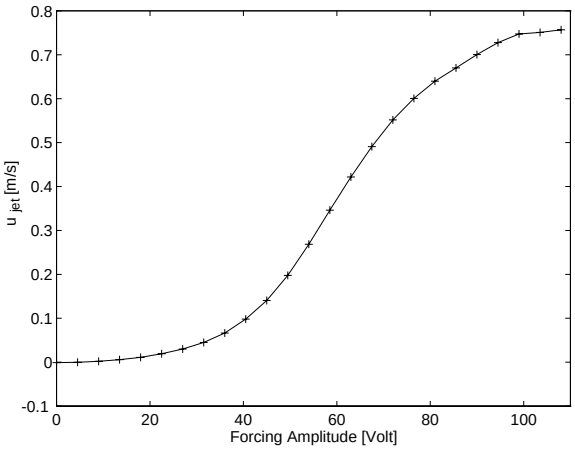

Figure 3.4: Integral jet velocity u_{jet} over forcing voltage amplitude at actuator resonant frequency f_r = 500 Hz = $0.1f^*$

With the absence of a outside flow, the performance of the actuator is shown in Figure 3.4 with the time averaged jet velocity u_{jet} over the input voltage. The emitting jet could reach velocities which were quite large in comparison to the velocities observed in the near wall region of a turbulent boundary layer, yet the actuator geometry was not optimal. A complete discussion of the flow modeling and optimization of membrane actuators is given in [3].

3.3 Instrumentation and Data Acquisition

Custom built constant temperature hot-wire anemometer were utilized to measure the streamwise velocity component. The frequency response of the hot-wires was more than 15 kHz, much higher than needed for the frequency range studied. The output voltage could be adjusted through different gain settings for matching the ±5 Volts range of the A/D converter.

The hot-wire probes consisted of a single platinum-rhodium wire, with a length to diameter ratio of approximately 200, welded between two prongs. The probe was mounted to the end of a long carbon fiber sting. The length of the sting was sufficient to place the probe out of the disturbed flow near the traverse. Each new probe was calibrated prior to a test series. Anemometer voltages were calibrated with pressure transducer voltages using a cubic polynomial. Drift from the calibrated velocities was checked periodically and the probe was recalibrated when necessary.

Data acquisition and reduction was performed in real time using an IBM-compatible PC-486. While acquiring a new data set through a 12 bit A/D converter, the signal conditioning and updating of the statistics of the previous set took place.

For acquiring the cross-correlation data presented in Section 4.3, a second, stationary hot-wire probe was fixed to the plate with the hot-wire approximately at $y^+ = 15$. The signal of both probes was then conditioned using a hardware high-pass filter at a cut-off frequency of 20 Hz. This enabled us to study only the correlation of the coherent structures and eliminated low-frequency correlations introduced for example by small fluctuations in the mean velocity.

3.4 Statistical Considerations

In order to study the effect of continuous forcing on a turbulent flow, it is necessary to consider long term average properties. According to classical theory of random data [12], average quantities converge like $1/\sqrt{N}$ where N is the total number of sampled data points. However, this is only true for uncorrelated data points. In a turbulent boundary layer, the correlation time is typically of the order of 100 t^* implying a sampling frequency (for this flow) of approximately 50 Hz. However, since the interest is also in capturing time-series data, a higher sampling frequency is required. A preliminary experiment was thus made to determine the appropriate number of data points necessary to ensure the accurate convergence of statistics using correlated data samples. As an example, the convergence of the average velocity as a function of total sampling time, T, is shown in Figure 3.5.

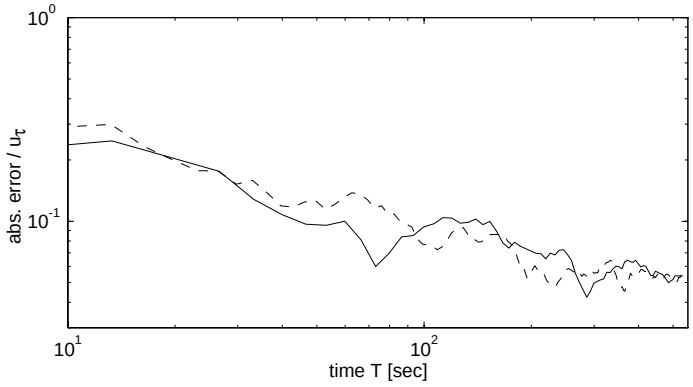

Figure 3.5: Convergence of the mean velocity at sampling frequencies $f_s = 7.5$ kHz (solid line) and $f_s = 15$ kHz (dashed) over sampling time T

Each curve represent the maximum absolute error from a total of ten runs taking approximately 500 seconds at two different sampling frequencies (7.5 kHz and 15 kHz). The measured values converge towards the "real" average (which was assumed to be the average of all ten runs at the maximum value of T). As can be seen, at these high sampling frequencies (relative to the "uncorrelated frequency" of 50 Hz), the error is essentially independent of the sampling frequency, but only depends on the total sampling time. On the basis of these results, the data presented is derived from one million data points sampled at 5 kHz and the errors in the mean were observed to be less than 0.08 u_τ.

Chapter 4

Results and Discussion

The actuator, flush mounted with the flat plate, was placed in a zero pressure gradient turbulent boundary layer $1.05m$ downstream of the flow tripping device. With a constant free-stream velocity $U_\infty = 6$ m/s for all experiments, the Reynolds number based on the momentum thickness at the actuator location was $Re_\theta \approx 1200$. The measured profiles of the first four statistical moments of the turbulent boundary layer were already shown in Figrure 2.2. They are in good agreement with standard boundary layer values [13]. The "wake" in the outer region of the mean velocity profile indicates a slightly negative, favorable, pressure gradient along the flat plate.

The inner length scale was $l^* = \nu/u_\tau \approx 55\mu$m (where ν is the kinematic viscosity) and $u_\tau = 0.28$ m/s is the friction velocity which are used for non-dimensionalization. The skin friction velocity was determined in a previous experiment using wall mounted shear-stress sensors [14].

With the hot-wire probe at one position, first the unforced flow statistics were measured and then, switching the actuator on, the forced case data was acquired. The actuator was run at a continuous forcing amplitude of 55 Volts at its resonant frequency throughout all experiments which resulted in a jet velocity of approximately $1\,u_\tau$. The locations referred to in the results are in a local coordinate system having its origin at the downstream end of the actuator.

4.1 Change in Turbulent Flow Spectrum

Figure 4.1 shows frequency spectra of the streamwise velocity component taken centerline at $x^+ = 60$ and $y^+ \approx 15$ downstream of the actuator end. The spectrum of the unforced case (solid line) corresponds well to those found in literature of turbulent flows. Forcing the boundary layer at the actuator's resonant frequency of 500 Hz ($0.10\,f^*$) takes place directly in the inertial range of the flow, which is given around the $-5/3$-slope of the spectrum [15]. In the forced case (dashed line) spectrum, the original forcing frequency can be seen only by a small remaining peak, while dissipation of the forcing energy into a wide frequency range can be observed. The energy cascades towards break-up into even smaller scales (higher frequencies) as well as introducing large scale structures in the range of the typical coherence and bursting frequencies.

4.2 Effect on Fluctuation Statistics

As an example of the effect of the forcing actuator on the profiles of the first four statistical moments, Figure 4.2 shows the near wall profiles of the undisturbed flow (solid line) and the forced (dashed) case at $x^+ = 60$ downstream of the actuator slit centerline. The unforced mean velocity profile was utilized to determine the unknown initial y-location of the hot-wire probe. The linear profile in the sublayer was extrapolated towards the wall and the data was shifted accordingly in the y-direction to match the no-slip conditions at the wall.

The location around $y^+ = 10...20$ is of particular interest, since in the unforced case the maximum peak in rms is approximately at $y^+ = 12$. The steep decrease in the skewness and the minimum in flatness are

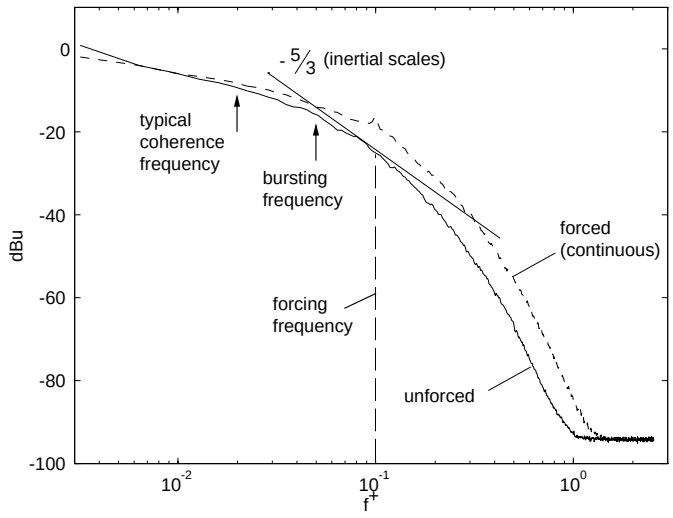

Figure 4.1: Frequency spectrum of the mean streamwise velocity $\overline{u}$ for the unforced (solid line) and forced (dashed) case at $x^+ = 60, y^+ \approx 15, z^+ = 0$

also approximately located at this position. The same identity of location is true for the forced case with the only difference that now the location is at $y^+ = 20$, where in addition the maximum change in mean velocity is present. Around that position the forced case profiles approach these of the unforced case.

Near the wall it is important to note that the two profiles almost match, indicating that the displacement at higher values of y^+ is not due to separation of the flow from the wall when being forced (which is blowing into and with it destabilizing the flow), but probably due to the vortical structures induced by the actuator. It seems that the profiles themselves keep their approximate shape but are stretched in the direction normal to the wall. Since the area of maximum turbulent production is often associated with the location of the maximum peak of the second-order statistical moment (*rms*), at least the position of this production is influenced. Since only continuous forcing was applied to the flow, an effect on the turbulence intensity was not expected in a dramatic way. The intensity of the *rms*-value is decreased in one area and increased in another, and the overall effect might cancel out.

For further discussion only the absolute change (in contrast to relative changes), i.e. the *difference* between the forced and the unforced case, is utilized to characterize the effect of the actuator. Thus, an increase in any flow statistics when forcing is applied is given by positive, a decrease by negative numbers. For a definition of the velocities used to characterize the statistics (i.e. u_{rms}, u_{skew}, and u_{flat}) see Equation (2.29). The profiles of the first four statistical moments shown in Figure 4.2 might be better to understand the physics. However, the contour plots presented next are helpful to study the spanwise extent of the area which is affected by the vortical structures.

Figures 4.3 to 4.5 show contour plots of the changes in fluctuation statistics in a yz-plane perpendicular to the streamwise direction. The original grid for data acquisition consisted of 30 locations in y by 9 locations in z on only one side of the actuator centerline. Previous scans (in z-direction only, at different heights y) showed that the flow field is symmetrical with respect to the centerline. For better understanding the data matrix was reflected at the $z^+ = 0$ axis. One row of zeros was added to the data matrix to match the boundary condition at the wall and a two-dimensional Gaussian filter was then applied to smooth the data.

The absolute change of the normalized mean velocity Δu^+ from the unforced to the forced case at two different positions downstream of the actuator is shown in Figure 4.3. The decrease in mean velocity (at $y^+ \approx 20, z^+ = 0$) and the increases, on either side in spanwise direction (at $y^+ = 5...10, z^+ = \pm(20...40)$), with only half the magnitude are indications of two counter-rotating streamwise vortical structures produced by the jet emitting from the actuator slit. Low-speed fluid is lifted upwards by the two vortices at the centerline and high-speed fluid is transported to lower speed regions on the outer side of the vortices. The diameter of the vortices is estimated to be approximately $20\,l^*$ at the end of the actuator slit.

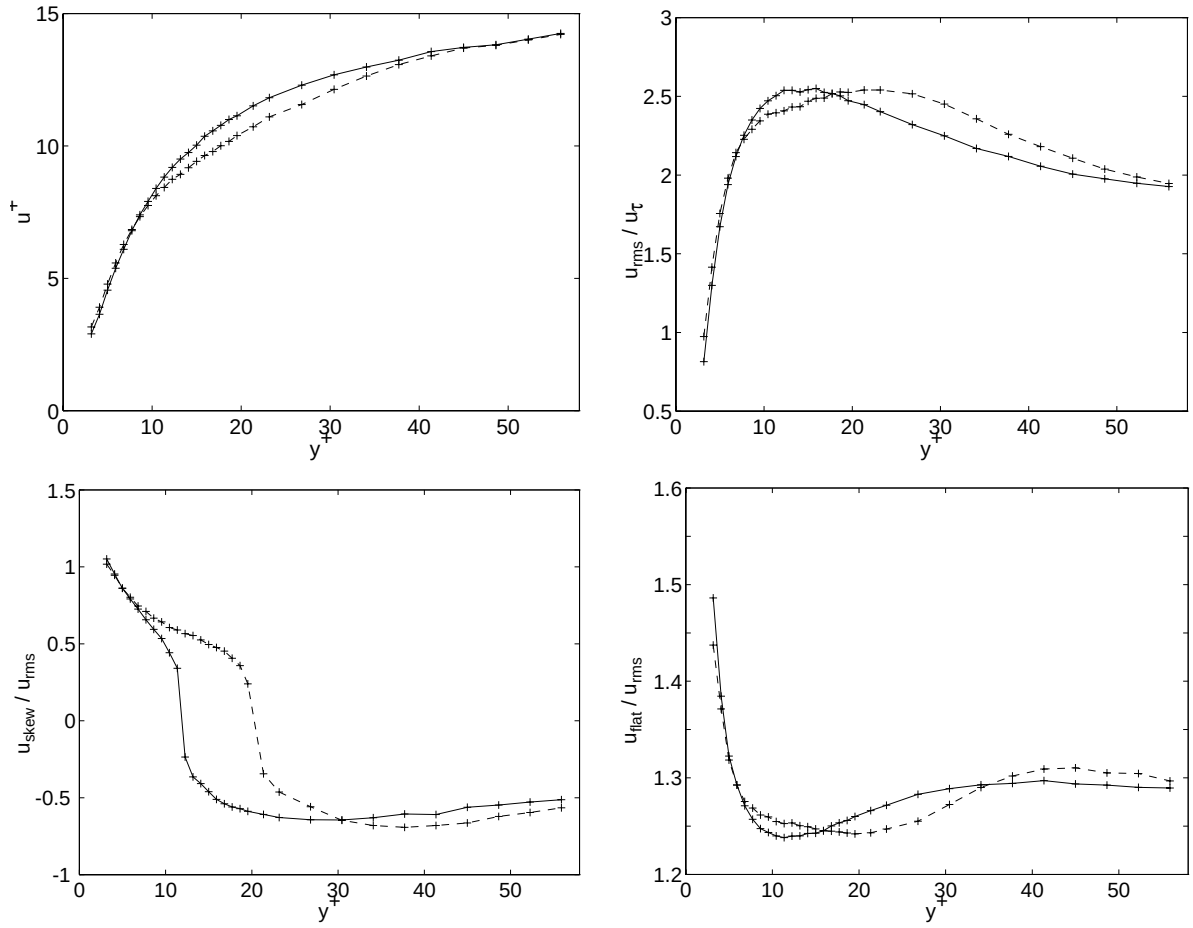

Figure 4.2: Near-wall profiles of the first four statistical moments of the streamwise velocity ($x^+ = 60$, $z^+ = 0$; solid line: unforced, dashed line: forced)

Jacobson, using an actuator with similar characteristics (in a laminar boundary layer), described vortices with about the same dimensions [1]. The emitting jet from the actuator slit with a width of only $1.5\,l^*$ induces two vortices which are much larger in diameter. The small scale forcing with high frequencies is clearly rectified into larger scales.

As can be seen by the location of the maximum negative change, the vortical structures are lifted up into outer regions of the boundary layer while convecting downstream. The inclination angle of the vortices was calculated to be $\theta_v \approx 5°$ against the wall. The vortices are also diverging in spanwise direction, which can be explained by potential theory in which two counter rotating vortices tend to separate. The reduction in magnitude of the changes in mean velocity is due to dissipation caused by the mixing motion of the turbulent flow. Yet, the vortical structures are quite stable. The effect of the vortices could clearly be seen as far downstream as $250\,l^*$ from the actuator end.

Figure 4.4 shows the absolute change $\Delta(\sqrt{\overline{u'^2}}/u_\tau)$ (change in *rms*) from the unforced to the forced case at two downstream positions. The field structure is more complex, however the upwards convection and dissipation described previously can also be observed. There are three distinct areas each for increase and decrease of the *rms* value. Worth noting is, that the decreased areas are all located on one level at $y^+ \approx 15$, where in the unforced, regular turbulent boundary layer the maximum *rms* is located and with it the maximum production of turbulence.

Figure 4.5, where the change in skewness $\Delta(u_{skew}/u_{rms})$ is shown, indicates clearly a very distinct area

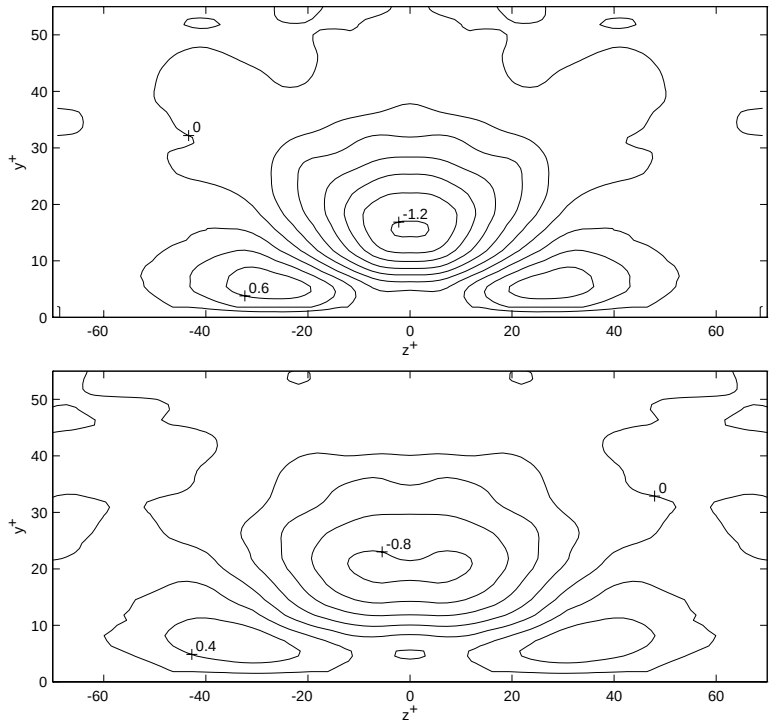

Figure 4.3: Contour plots of the absolute change in normalized mean velocity Δu^+ from the unforced to the forced case at $x^+ = 10$ (top) and $x^+ = 60$ (bottom)

of the actuator effect on the skewness. The high density of contour lines implies large changes, which are towering out of a plane of almost zero change. However this is mainly due to the very steep gradient in the unforced skewness profile at $y^+ \approx 12$ (see Figure 4.2). The near wall edge of the affected area therefore stays almost constant, as well as the intensity of change. A lift-up in the change of the skewness can only be seen by the increased size in y and a more moderate roll-off towards higher y^+. However, the spanwise extent does not depend upon the steep gradient in the skewness profile. The slope is less steep in spanwise direction but shows clearly the limited area of influence.

As a summary, Figure 4.6 shows the change of all four statistical moments at the centerline ($z^+ = 0$) and at different locations downstream. The decrease in magnitude as well as the upward displacement when going downstream can be seen clearly. Although the data presented furthest downstream is at $x^+ = 140$ the effect of the vortical structures could be seen as far downstream as $x^+ = 250$. The inclination angle $\theta_v \approx 5°$ presented earlier in this paper was calculated using the displacement of the maximum negative change in mean velocity in y-direction over streamwise position x^+.

4.3 Cross-Correlation Measurements

The production of turbulence is attributed to the presence of coherent structures emerging from low-speed fluid being lifted up into higher speed flow as discussed in Section 2.2.2. To investigate the effect of small scale forcing on these coherent structures, space-time correlation measurements were performed. One hot-wire probe was kept at a fixed position on the centerline $x^+ = 60$ downstream of the actuator at about $y^+ \approx 15$. The location in y-direction was determined as described in 4.3.2. Since the fixed hot-wire couldn't been calibrated, cross-correlation measurements were only done with the voltage output. However, both hot-wires had the same dimensions and with it the same voltage output. It is therefore assumed that the response of both probes, the approximate range and statistics, was roughly matched. The second, free hot-wire probe was placed on the traverse, and could be used for velocity measurements at all locations. The separating

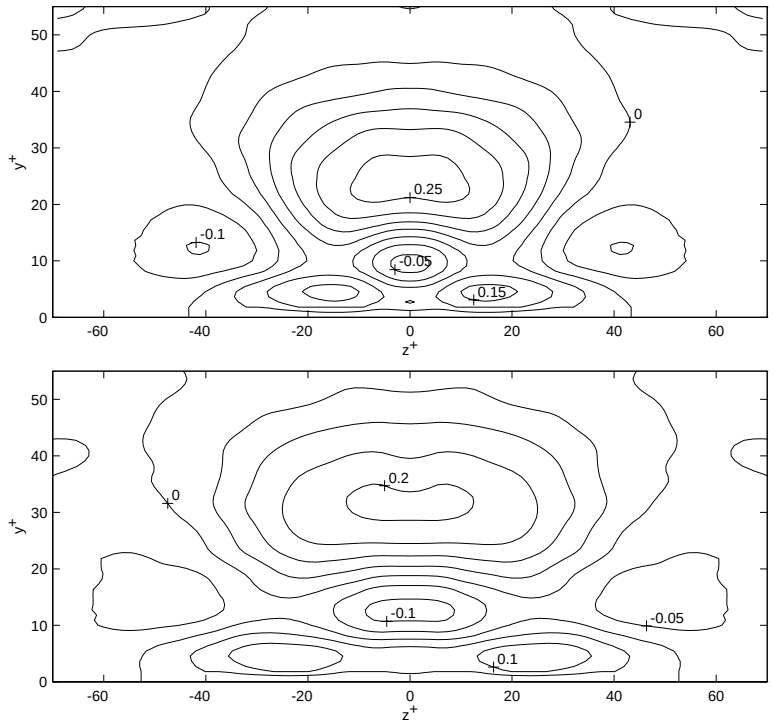

Figure 4.4: Contour plots of the absolute change of the normalized second-order statistical moment $\Delta(u_{rms}/u_\tau)$ (root-mean-square) from the unforced to the forced case at $x^+ = 10$ (top) and $x^+ = 60$ (bottom)

distance between the probes is denoted by Δx^+, Δy^+, and Δz^+ for the three directions in space.

4.3.1 Correlation in Streamwise Direction

As a first approach towards the effect on coherent structures by forcing the turbulent boundary layer, the cross-correlation in streamwise direction was investigated. Initially the two hot-wire probes were positioned close together ($\Delta y^+ \approx 12$) with no streamwise separation as shown in Figure 4.7. The free probe was then traversed upstream in steps of approximately $10\,l^*$. The blockage of the free (upper) probe was realized but not found to be significant since the correlation curves show no evidence of reduced correlation or other disturbances.

One example of the cross-correlation measurements made in streamwise direction is shown in Figure 4.8, with $\Delta x^+ = 10$, to compare the unforced (solid line) and the forced (dashed line) case. The location τ^+_{max} of the peak value of $(R_{uu})_x$ is shifted to a lower value in the forced case. This is due only to the separation of the hot-wires in y and already indicates a change in the inclination angle of the coherent structures, better seen in the cross-correlation in y-direction. The magnitude of the maximum correlation value stays almost constant and the shape of the correlation curve is not altered.

Cross-correlation data of the unforced and forced case at several separating distances Δx^+ is given in Figure 4.9. Compared to the results in y- and z-direction discussed later, the maximum peak values of $(R_{uu})_x$ decreases only slightly with increasing Δx^+ and also stay almost constant in magnitude when being forced. The peak moves to the right with increasing Δx^+.

Plotting the offset location τ^+_{max} of the peaks over hot-wire separation distance Δx^+ as shown in Figure 4.10 leads to the convection speed of the coherent structures. The streamwise convection speed is determined by the slope of the linear τ^+_{max}-Δx^+-lines well fitting the measured data. The fact that $\tau^+_{max} \neq 0$ at $\Delta x^+ = 0$ (and the maximum $R_{uu}(\Delta x^+ = 0) \not\approx 1$ in Figure 4.9) is due to the initial positioning of the two hot-wire probes as shown in Figure 4.7. The separation of the two hot-wires in y-direction was compensated

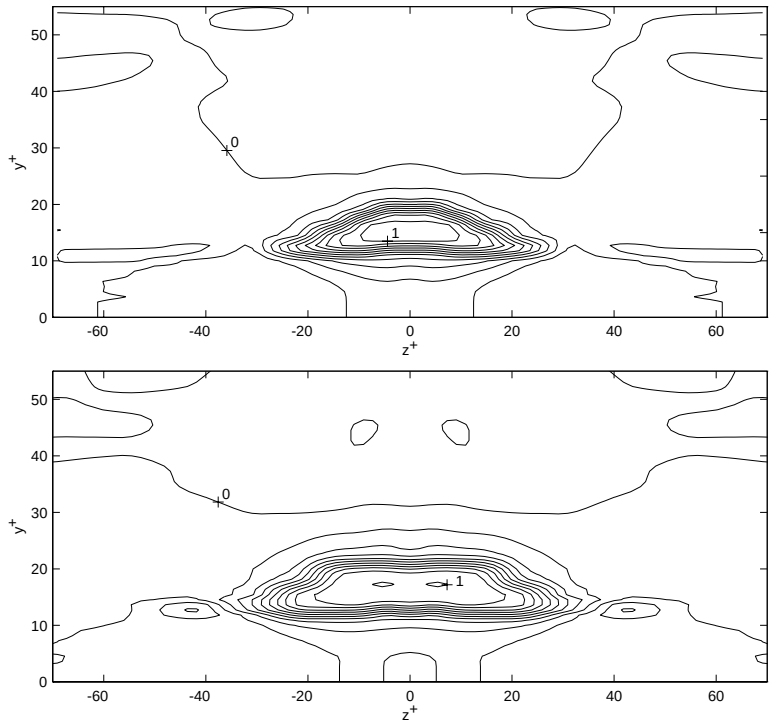

Figure 4.5: Contour plots of the absolute change of the normalized third-order statistical moment $\Delta(u_{skew}/u_{rms})$ (skewness) from the unforced to the forced case at $x^+ = 10$ (top) and $x^+ = 60$ (bottom)

for by subtracting the time delay between the two signals at the first, initial position, which places the fixed hot-wire to a virtual position at the same height as the free hot-wire probe of about $y^+ \approx 25$. This procedure also excludes the possible change of the inclination angle of the coherent structures when being forced.

Both the unforced and forced case show the same slope leading to a convection speed of $u_c = 10.8\,u_\tau$ at $y^+ \approx 25$. The convection speed falls within the range of these found by Johansson, Alfredsson and Kim [9], who determined a slightly lower speed of $10.6\,u_\tau$ in numerical simulations, and the convection speed of $13\,u_\tau$ found experimentally by Johansson, Alfredsson and Eckelmann [8]. Johansson, Alfredsson and Eckelmann also found in their experiments that u_c stays almost constant up to $y^+ \approx 30$. It is therefore assumed for the following discussions that the convection speed stays constant over the y^+-range studied in this paper for both the unforced and forced case.

4.3.2 Correlation in y-direction

Cross-correlation measurements in y-direction were performed in a similar way. The initial position of the two hot-wire probes was as described in the previous section, with the free probe approximately $\Delta y^+ = 12$ above the stationary probe. The free hot-wire probe was then traversed in y-direction in steps of approximately $4\,l^*$.

Figure 4.11 shows $(R_{uu})_y$ for a single value $\Delta y^+ = 12$ to compare the unforced (solid line) and the forced (dashed line) case. Again, as found in the streamwise correlation, the maximum correlation values in the unforced and forced case are almost the same and the shape of the graph is not altered. However, a shift to the left of the peak can clearly be seen when forcing is applied. There is no geometrical problem now concerning the positions of the hot-wire probes. The probes are in line at the same x- and z-location. Since the convection speed u_c is considered to be constant (as found in the previous section), this time shift is associated with a change of the inclination angle of the coherent structures. The negative time-shift indicates, with the hot-wire probes at the same location when the actuator is switched on, that with a now smaller offset of the peak the structure must be inclined with a higher angle against the wall in the forced

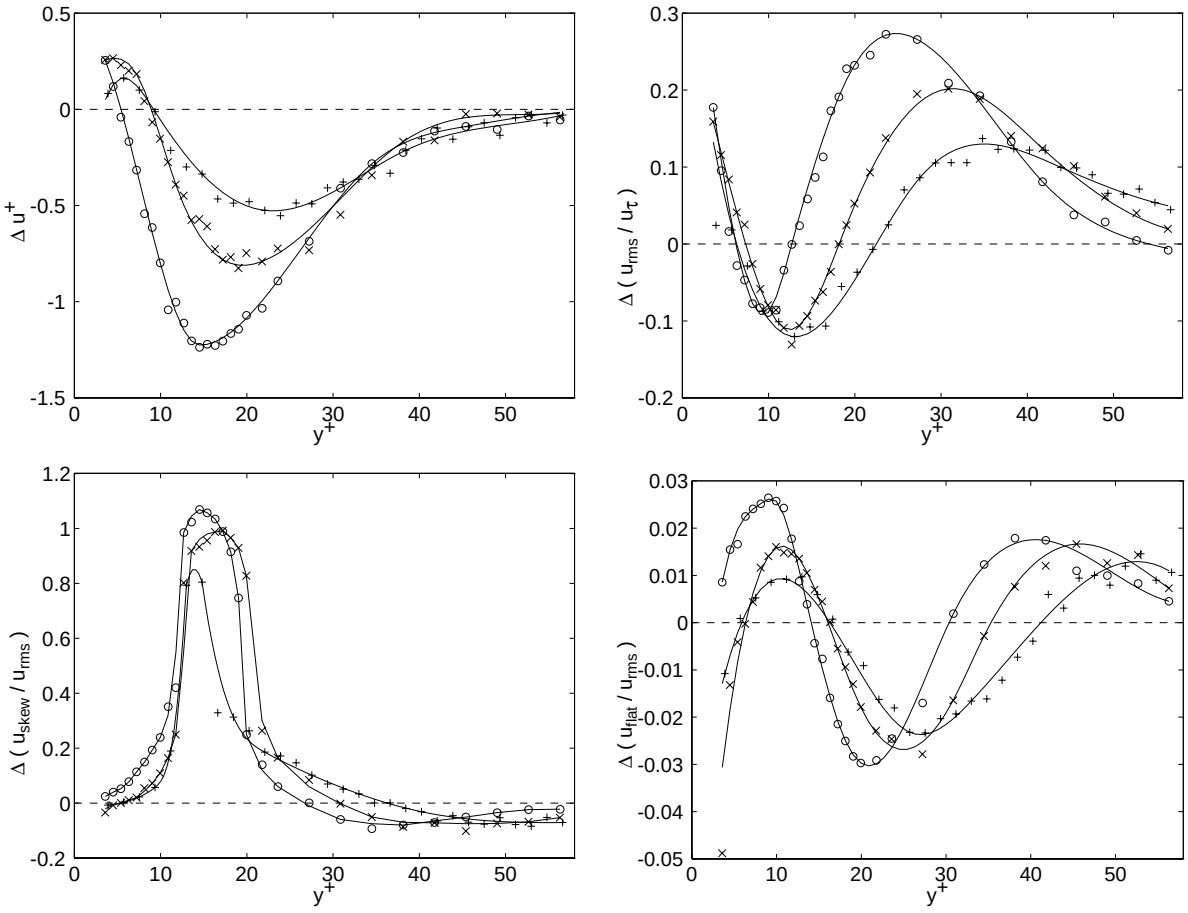

Figure 4.6: Absolute change of the first four statistical moments from the unforced to the forced case at centerline ($z^+ = 0$). $\circ$ $x^+ = 10$, $\times$ $x^+ = 60$, $+$ $x^+ = 140$

case.

Figure 4.12 shows a set of cross-correlation data for the unforced and forced case for several Δy^+. At higher values of $|\tau^+|$ the "tails" of the correlation graphs don't match as in the streamwise direction (Figure 4.8). The decay of the correlation with increasing Δy^+ is much faster and is shown explicitly in Figure 4.13 where the maximum correlation values are plotted over the wire separating distance.

These data points fit to an exponential decay law $(R_{uu})_y \propto e^{-k\Delta y^+}$, where $k = 0.0554$. All correlation data presented was non-dimensionalized with the auto-correlation of the fixed hot-wire probe only. Thus, the exponential curve reaches a $(R_{uu})_y \simeq 1$ when both hot-wire locations fall together ($\Delta y^+ = 0$). This procedure also determined the initial separating distance between the two hot-wires. With the known position of the free probe (given by the calibrated velocity measurement and look-up of the appropriate location in y from the velocity profiles) the initial separating distance, and with it the y-location of the stationary hot-wire probe could be determined.

In Figure 4.14, where the location τ^+_{max} of the peak values of $(R_{uu})_y$ is plotted versus the wire separating distance Δy^+, the data was shifted accordingly in y-direction. The linear fit of the unforced data then goes through zero. As can be imagined, the time shift between two signals at (virtually) the same location should be zero, and the cross-correlation therefore represents the auto-correlation at that position.

With a given constant convection speed u_c from the previous section, the average inclination angle of the coherent structures at the height between the two hot-wire probes is given by $\theta = \tan^{-1}(u_c \tau^+_{max}/\Delta y^+)$. For the unforced case, the inclination angle stays almost constant at $\theta_u \approx 20^\circ$ up to $y^+ \approx 50$, supported by the

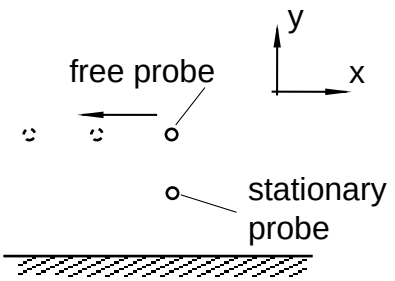

Figure 4.7: Initial positioning of the hot-wire probes for acquiring cross-correlation data in streamwise direction

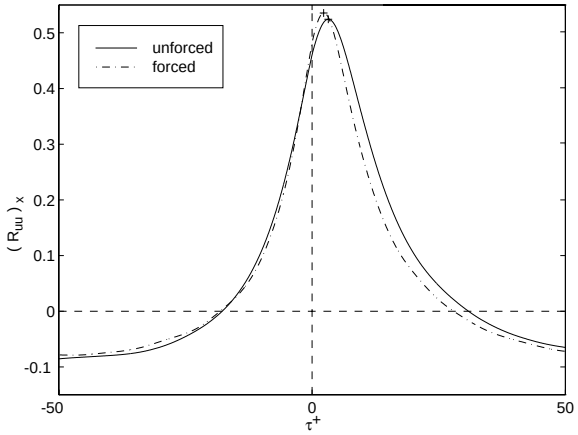

Figure 4.8: Comparison between unforced (solid line) and forced (dashed) case cross-correlation in streamwise direction for $\Delta x^+ \approx 10$

unforced τ^+_{max}-Δy^+-line well fitting the measured data. Johansson, Alfredsson and Eckelmann [8] found in their experimental investigations a maximum inclination angle of 20° in the buffer region at $y^+ = 20$.

Keeping the two hot-wires at the same position (i.e. $\Delta y^+ = const.$) and switching the actuator on, the location of the maximum $(R_{uu})_y$ experiences a shift to a lower τ^+_{max} from the unforced to the forced case. This time shift is present over a wide range of Δy^+. It indicates an increase of the inclination angle when forcing the turbulent boundary layer. With geometrical considerations as shown in Figure 4.15 , the inclination angle is found to be increased more close to the wall and less increased at higher y^+, approaching the unforced inclination angle. The forced inclination angle ranges from approximately 30° where the probes are close together ($\Delta y^+ \approx 15$) to an inclination angle of only 22° at $\Delta y^+ \approx 35$. The decrease in the change of the inclination angle in the forced case might also be attributed to an averaging effect when measuring across a wider separation distance of the hot-wires.

Figure 4.16 shows the peak value of $(R_{uu})_y$ over its location τ^+_{max}. The forced case peaks are always at a lower τ^+_{max} suggesting a breakup of the coherent structures. This is supported by the spectra shown in Figure 4.1 where the forced case spectrum shows the presence of more dissipation.

4.3.3 Correlation in Spanwise Direction

For investigating the spanwise cross-correlation, the free hot-wire probe was positioned next to the fixed probe at the same $x^+ = 60$ and $y^+ \approx 15$. The given spanwise distances Δz^+ are taken from centerline to centerline of the hot-wire probes, hence the relatively large initial $\Delta z^+ \approx 24$. The free hot-wire probe was traversed in steps of approximately $4\,l^*$ on one side of the actuator centerline only. The spatial resolution is restricted by the hot-wire length (about $10\,l^*$) since an averaging effect is probably given.

One example ($\Delta z^+ = 35$) to compare the unforced and forced case correlation is given in Figure 4.17.

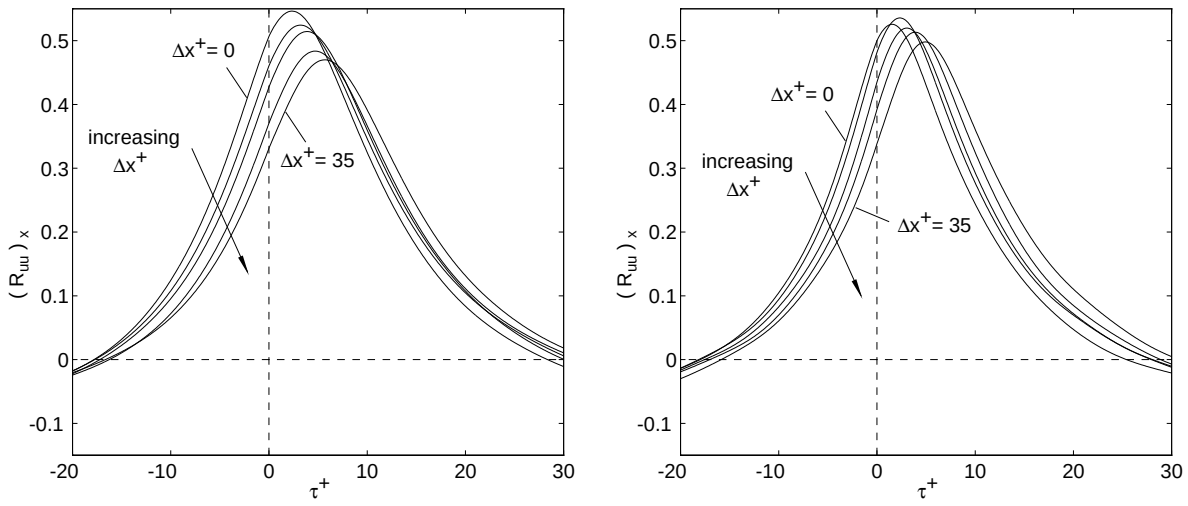

(a) unforced

(b) forced

Figure 4.9: Cross-correlation in streamwise direction for $\Delta x^+ \approx 0...35$ in steps of approx. $10\,l^*$; a) unforced case, b) forced case

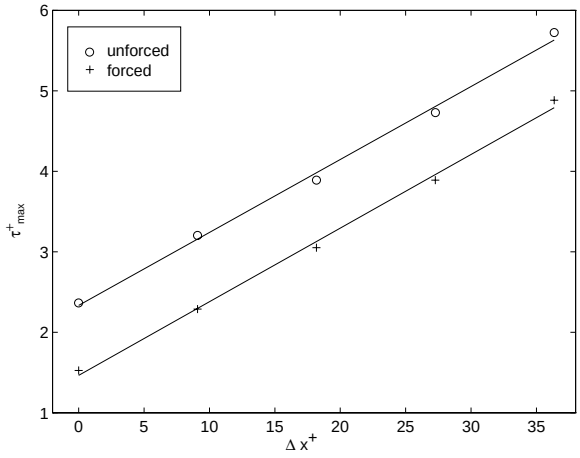

Figure 4.10: Location of maximum cross-correlation τ^+_{max} in streamwise direction over wire separation distance Δx^+

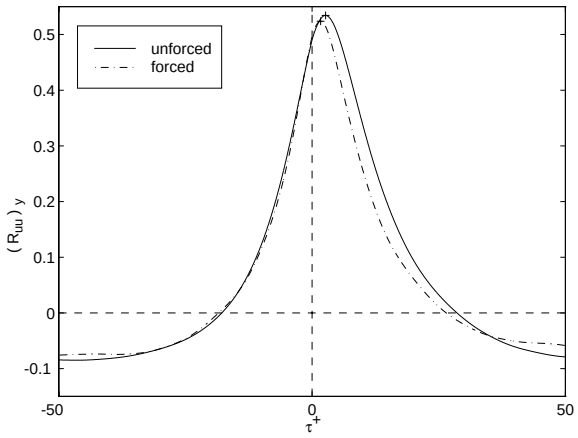

Figure 4.11: Comparison between unforced (solid line) and forced (dashed) case cross-correlation in y-direction for $\Delta y^+ \approx 12$

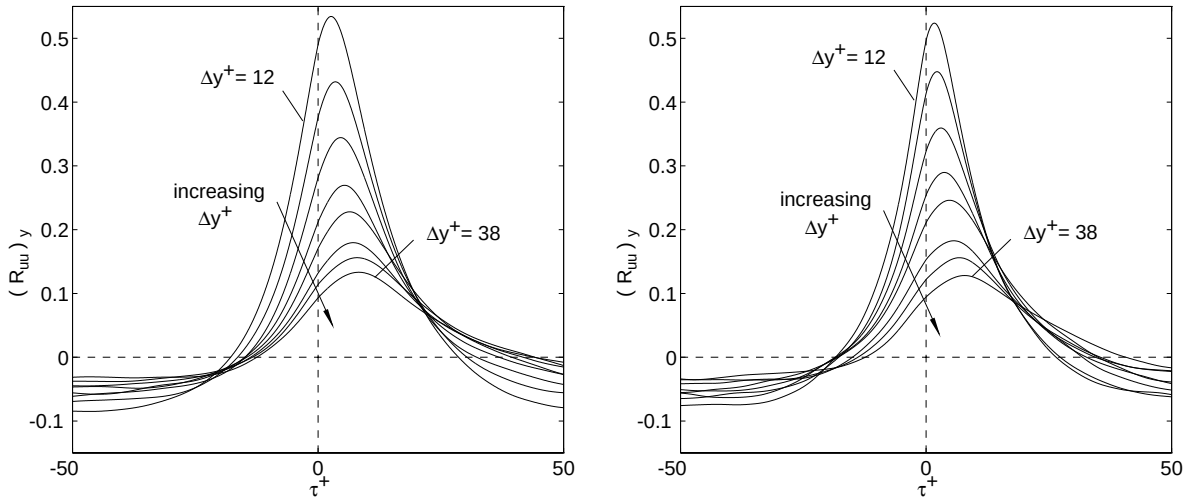

(a) unforced

(b) forced

Figure 4.12: Cross-correlation in y-direction normal to the wall for $\Delta y^+ \approx 12...38$ in steps of approx. $4\,l^*$; a) unforced case, b) forced case

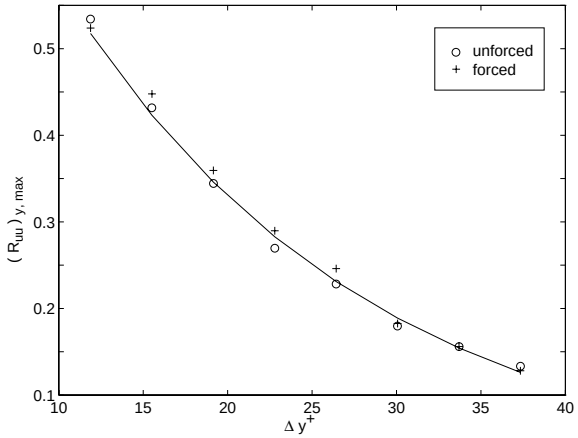

Figure 4.13: Maximum correlation value in y-direction normal to the wall $(R_{uu})_{y,max}$ over wire separation distance Δy^+

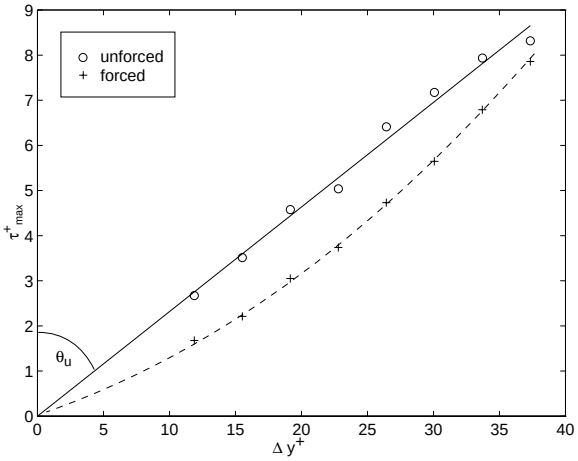

Figure 4.14: Location of maximum cross-correlation τ^+_{max} in y-direction normal to the wall over wire separation distance Δy^+

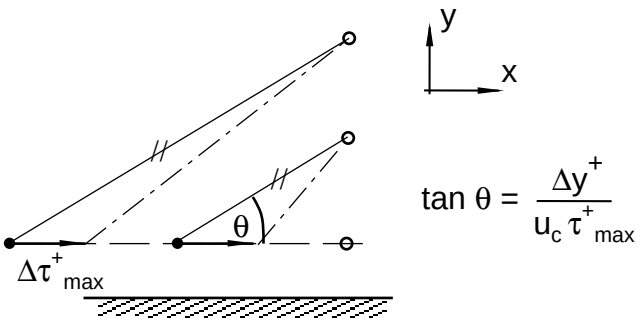

Figure 4.15: Geometrical considerations to determine the change in inclination angle θ of the coherent structures when being forced (solid line: unforced, dashed line: forced)

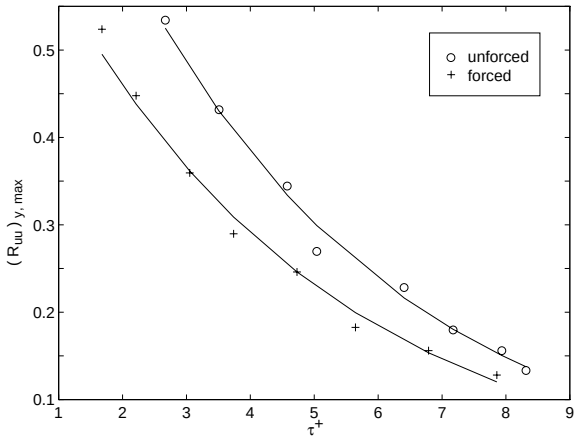

Figure 4.16: Maximum correlation value $(R_{uu})_{y,max}$ in y-direction over correlation time τ^+

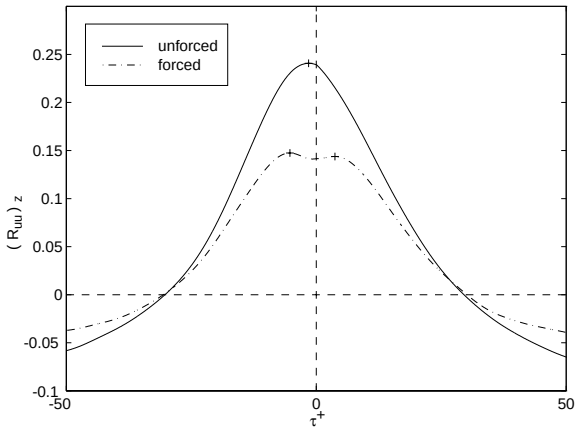

Figure 4.17: Comparison between unforced (solid line) and forced (dashed) case cross-correlation in spanwise direction for $\Delta z^+ \approx 35$

The unforced case (solid line) correlation shows no specific features except that the peak of the maximum correlation is at a negative τ^+. The forced case (dashed line) however shows reduced correlation and exhibits two peaks, which are almost symmetrical with respect to $\tau^+ = 0$.

Plotting several cross-correlation data in z-direction for the unforced and forced case (Figure 4.18) shows the development of this behavior. At smaller values of Δz^+ both cross-correlations, the unforced and forced case, exhibit only one peak and the location is almost perfectly at $\tau^+_{max} = 0$. Increasing the distance between the two hot-wires, the peak in the unforced case correlation is shifted to negative τ^+. The correlation curves are then observed to develop two maxima which are symmetrical with respect to $\tau^+ = 0$.

However, two very interesting phenomena occur: the peak of the correlation in the forced case does not shift to one side before separating into two peaks, which are in addition developing earlier, that is at a lower Δz^+. The forced case cross-correlation (at small Δz^+) is in general smaller in absolute magnitude than in the unforced case. As in the y-direction, the correlation decreases rapidly with increasing wire separation Δz^+ and the "tails" at higher $|\tau^+|$ are spread further apart. The spanwise extent (or diameter) of the coherent structures can be estimated by the Δz^+ for which the correlation at $\tau^+ = 0$ first crosses zero. For both the unforced and forced case this is true at $\Delta z^+ \approx 50$. As shown earlier (in the contour plots of the changes in mean velocity Figure 4.3) the diameter of one introduced vortex (at the same downstream location where the correlation data was taken, i.e at $x^+ = 60$) was found to be about 20...30 l^*. An averaging effect across the hot-wire length might account for this difference. However, the numbers are of the same order of magnitude

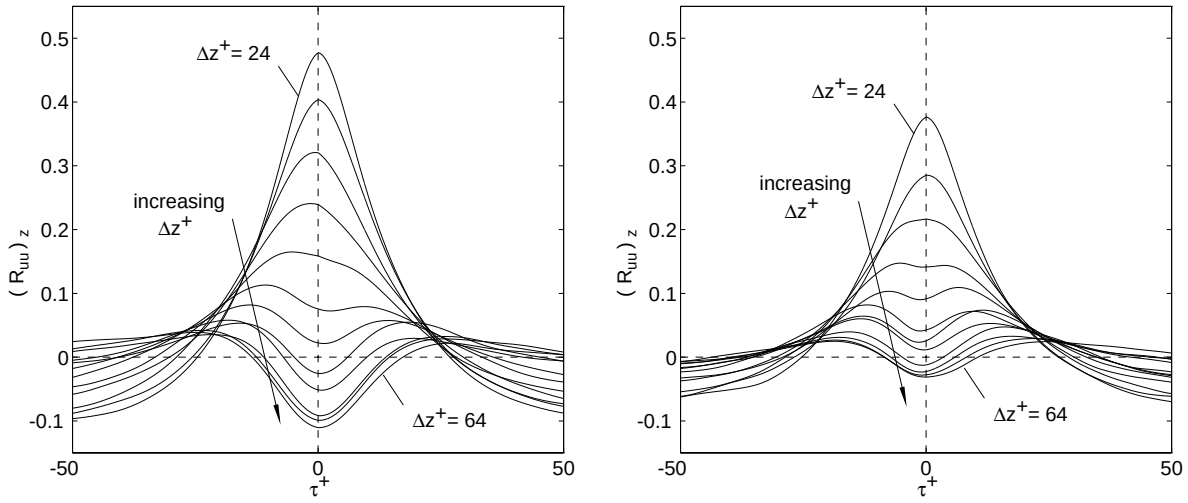

(a) unforced

(b) forced

Figure 4.18: Cross-correlation in spanwise direction for $\Delta y^+ \approx 24...64$ in steps of approx. $4\,l^*$; a) unforced case, b) forced case

and similar to those found by Johansson, Alfredsson and Kim [9].

In Figure 4.19, the locations τ^+_{max} of the maximum correlation value is plotted versus wire separation distance Δz^+. With the same technique used to calculate the inclination angle θ of the coherent structures against the wall, the sideways angle (or yaw angle) of the structures (see Figure 2.3) is found to be $\Phi_u \approx \pm 8°$ against the streamwise centerline to both sides. The structures can be tilted to one side or the other, hence the two peaks in the correlation curves. Forcing the flow increases this angle slightly. A separation into two peaks can be seen first at $\Delta z^+ \approx 42$ for the unforced case, and $\Delta z^+ \approx 35$ for the forced case.

The slightly increased yaw angle of the coherent structures when being forced could explain the earlier detection of two peaks in the spanwise correlation. The lower correlation peak values in the forced case suggest that the forcing breaks up the existing structures. This break-up is also supported by the forced case spectrum presented earlier. Thus, the coherent structures, and with them the production of turbulence, is directly influenced by the actuator.

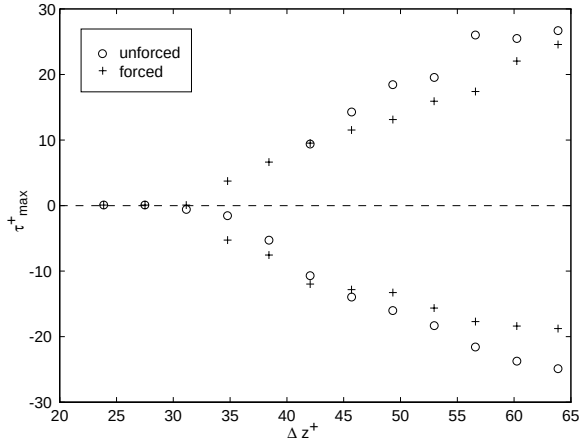

Figure 4.19: Location of maximum cross-correlation τ^+_{max} in spanwise direction over wire separation distance Δz^+

Chapter 5

Conclusions and Outlook

Small-scale forcing of a turbulent boundary layer utilizing a resonant membrane actuator was investigated. The emitting jet from the actuator exit slit introduced two counter-rotating vortical structures convecting downstream with the main flow. The effect on the flow statistics as well as the coherent structures present in turbulent flow was studied. Hot-wire anemometry and two-point space time correlation measurements were performed to characterize the flow field.

Forcing took place at the actuator's resonant frequency which falls within the inertial range of the turbulent flow. Spectrum analysis showed that the forcing energy is distributed over a wide frequency range. In the forced case spectrum, break-up into even smaller scales was observed. More important however is the introduction of larger scale structures by the very small jet.

Continuous forcing of the turbulent boundary layer has an significant effect on the fluctuations statistics. The transport of fluid packets in the near wall region by the two counter-rotating vortices could be examined. Further, a spatially limited effect on the skewness and an effect on the *rms*-distribution was found. Flow field mapping at several downstream location showed the dissipation due to turbulent mixing. Decreasing magnitude of the effects as well as its divergence in spanwise and y-direction was observed.

A well-defined and repeatable influencing effect was also examined on the coherent structures. For the unforced case, their properties, such as inclination angle and propagation speed, were in good agreement with those found in literature. Forcing the turbulent boundary layer showed no effect on the propagation speed, it stayed constant at $u_c = 10.8\, u_\tau$. The inclination angle however has been increased and the coherent structures were bent into a kind of sausage-shaped form. The inclination angle of the coherent structures was found to be increased to $\theta \approx 30°$ close to the wall and approaching the unforced case inclination angle at higher y^+. The yaw angle was also slightly increased. The detection of two peaks in the spanwise correlation, attributed to the sideways orientation of the structures, was earlier in the forced case. Reduced correlation in spanwise direction suggests a break-up of the coherent structures which is additionally supported by the characteristics of the forced case spectrum.

Since coherent structures are coupled with a major part of turbulence production, small-scale forcing is considered to be a good approach for turbulence control. Direct effects on these structures could be clearly seen. However, in this study the performance for turbulence reduction is far from being effective. For example a decrease in *rms* of only about 5% has been examined at some locations. The increase in the near-wall inclination angle of the coherent structures when being forced could be followed by a reduction in wall shear stress.

Continuous forcing might not be optimal, however it can lead to a good understanding of the changes in turbulent boundary layer flow. Amplitude modulation and different exit slit geometries should be examined in future investigations. The more advanced technique of upstream detection of structures worth influencing and feed-back control of the performance of the actuator with downstream sensors is currently investigated and shows first promising results. The implementation of independent actuator arrays, manufactured inexpensively in large quantities using MEMS technology, with integrated sensors and hard-ware control processors would be the ultimate goal for turbulence control.

Bibliography

[1] S.A. Jacobson and W.C. Reynolds. An experimental investigation towards the active control of turbulent boundary layers. *Thermosciences Division Report No. TF-64, Department of Mechanical Engineering, Stanford University*, 1995.

[2] R.D. Wiltse and A. Glezer. Manipulation of free shear flows using piezo actuators. *J. Fluid Mech.*, 249:261–285, 1993.

[3] R. Rathnasingham and K.S. Breuer. Characteristics of resonant actuators for flow control. *AIAA-96-0933*, 1996.

[4] H. Schlichting. *Boundary Layer Theory.* McGraw-Hill, Inc, New York, New York, 1968.

[5] F.M. White. *Viscous Fluid Flow.* McGraw-Hill, Inc., New York, New York, 1991.

[6] S.J. Kline, W.C Reynolds, F.A. Schraub, and P.W. Runstadler. The structure of turbulent boundary layers. *J. Fluid Mech.*, 30:741–773, 1967.

[7] R.F. Blackwelder and R.E. Kaplan. On the wall structure of the turbulent boundary layer. *J. Fluid Mech.*, 76:89, 1976.

[8] A.V. Johansson, P.H. Alfredsson, and H. Eckelmann. On the evolution of shear-layer structures in near-wall turbulence. In *Advances in Turbulence.* Springer Verlag, 1987.

[9] A.V. Johansson, P.H. Alfredsson, and J. Kim. Evolution and dynamics of shear-layer structures in near-wall turbulence. *J. Fluid Mech.*, 224:579–599, 1991.

[10] W.S Saric. Turbulent boundary layers in subsonic and supersonic flow. Technical Report 335, AGARD, 1996.

[11] M.E. Grimaldi. Roughness-induced boundary layer transition. Master's thesis, Massachusetts Institute of Technology, 1994.

[12] J.S. Bendat and A.G. Piersol. *Random Data: Analysis and Measurement Procedures.* Wiley-Intersciences, New York, New York, 1971.

[13] A.V. Johansson, J.Y. Her, and J.H. Haritonidis. On the generation of high-amplitude wall-pressure peaks in turbulent boundary layers and spots. *J. Fluid Mech.*, 175:119–142, 1987.

[14] R. Rathnasingham. Ph.d. thesis (not published yet).

[15] K.S. Breuer. Personal communication.